THE ASTROPHYSICAL JOURNAL, 326:954–966, 1988 March 15

MAGNETIC FIELD STRUCTURE OF THE STAR-FORMING REGION W3(OH): VLBI SPECTRAL LINE RESULTS

J. A. GARCÍA-BARRETO
Instituto de Astronomía, Universidad Nacional Autónoma de México; and Research Laboratory of Electronics, Massachusetts Institute of Technology
B. F. BURKE
Research Laboratory of Electronics, Massachusetts Institute of Technology
M. J. REID AND J. M. MORAN
Harvard-Smithsonian Center for Astrophysics
A. D. HASCHICK
Haystack Observatory; and Harvard-Smithsonian Center for Astrophysics
AND
R. T. SCHILIZZI
Netherlands Foundation for Radio Astronomy
Received 1987 June 29; accepted 1987 September 14

ABSTRACT

We have conducted a six-station, very long baseline interferometric (VLBI) observation of the ground state 1665 MHz OH emission source in W3(OH) with full polarization information. We have been able (1) to produce spectral line VLBI synthesis maps in all Stokes parameters; (2) to identify several Zeeman pairs; (3) to determine the percent of linear, circular, and total polarization of the emission of each feature; and (4) to infer some information about the three-dimensional structure of the magnetic field.

Eighty-one maser components stronger than 1.5 Jy were detected. Sixty-five exhibited pure circular polarization: 46 were left circularly polarized and 19 were right circularly polarized. Sixteen features had elliptical polarization. Ten of these features were more than 70% polarized and had more circular polarization than linear polarization. Six features were less than 60% polarized, and three of these had linear polarization greater than circular polarization. The partially elliptically polarized features may be σ components with intrinsic Faraday rotation inhibiting the growth of linear polarization. Five Zeeman pairs were detected. The line widths varied from 0.15 km s^{-1} to 0.55 km s^{-1} and showed no clear correlation with strength, polarization, or size of the maser feature. No features were detected having "pure" linear or unpolarized emission that might have been identified as π components.

Our observations suggest that the OH cloud is permeated with a magnetic field having an average strength of 6 mG pointing away from Earth and with a SE–NW projected orientation on the plane of the sky.

Subject headings: interferometry — interstellar: magnetic fields — masers — nebulae: individual (W3) — polarization — Zeeman effect

I. INTRODUCTION

Magnetic fields are believed to play a major role in the dynamics of astronomical phenomena and particularly in the star formation process. In general, we wish to know the magnetic field strength and its (three-dimensional) orientation, and how the vector field varies in different parts of a source. Earlier observations have shown that the magnetic field strength varies over a wide range. The general galactic field is a few microgauss, increasing in strength to a few tens of microgauss in giant molecular clouds (Verschuur 1974; Troland and Heiles 1982). In the dense molecular material near compact H II regions, the field can be several milligauss (Lo *et al.* 1975; Moran *et al.* 1978).

The OH maser emission from W3(OH) is highly polarized, and the maser spots are spread across a 2″ field projected against a compact H II region. A Stokes parameter analysis of the spectrum of the OH emission in the 1665 MHz transition was published by Meeks *et al.* (1968) and by Coles, Rumsey, and Welch (1968). Most of the features are 100% circularly polarized, but some are partially elliptically polarized. From a study of the circular polarization of the OH maser emission in many transitions, Davies (1974) concluded that the polarization was due to the Zeeman effect with a magnetic field strength of about 5 mG. Subsequently, a map of the 6035 MHz transition made by Moran *et al.* (1978) showed that many pairs of oppositely polarized spectral features were spatially coincident, thereby greatly strengthening the Zeeman hypothesis. At 1665 MHz, the maser emission has been mapped in one sense of linear polarization by Reid *et al.* (1980), who identified 70 components, and in right and left circular polarization by Norris, Booth, and Diamond (1982), who identified 88 components. Reid *et al.* (1980) found that the maser spots had typical angular sizes of 0″.005 although 25% were unresolved and smaller than 0″.003 (10^{14} cm at a distance of 2.5 kpc). The masers were clumped in about a dozen clusters each about 2×10^{15} cm in size. Each cluster has a mean velocity of about -44 km s^{-1} and a range in velocity of about 4 km s^{-1}. These apparent velocity shifts are probably due to the Zeeman effect in a field of 5 mG. Although the flux densities of the maser features are variable in time, the dominant features have not

1988ApJ...326..954G

changed greatly in the time span of about two decades over which it has been observed (e.g., compare the data in this paper with Moran *et al.* 1968 and Barrett and Rogers 1966). The velocity shift between the OH masers and the star, as deduced from recombination line measurements, suggests that the OH maser emission may arise from a remnant accretion shell (Reid *et al.* 1980; Garay, Reid, and Moran 1985). However, the best estimate of the stellar velocity is about -46 ± 1 km s^{-1} (Berulis and Ershov 1983; Welch and Marr 1987) when non–LTE effects are accounted for in the recombination line measurements. Hence, the infall velocity of the OH masers is small, probably between 0 and 3 km s^{-1}.

All the previous imaging observations were performed with limited polarization information. We therefore decided to obtain a complete map of the OH maser emission in all Stokes parameters in order to study more fully the structure of the magnetic field in the region. In this work, we report the results of a VLBI aperture-synthesis experiment on the 1665 MHz emission in the $^2\Pi_{3/2}$ $J = 3/2$, $F = 1$–1 transition from W3(OH). In § II we describe the observation and analysis. The results of the analysis are given in § III, and discussion and summary are contained in § IV.

II. OBSERVATION, CALIBRATION, AND ANALYSIS

a) Observations

The VLBI observations were performed on 1978 September 29–30. We used six stations: five within the continental United States and one at the Dwingeloo Observatory in the Netherlands (see Table 1). The US stations received both right-hand (RCP) and left-hand (LCP) circular polarizations. Dwingeloo received linear polarization only, and its data were not included in the polarization analysis. The network used for the polarization analysis was composed of the stations at OVRO in California, Haystack in Massachusetts, NRAO[1] in West Virginia, GRAS in Texas, and VRO in Illinois.

The interferometer data were collected on the Mark II recording system and processed on the NRAO correlator in Charlottesville, Virginia. At each station, the recorded data stream was switched once per second between RCP and LCP. This was accomplished at Haystack, GRAS, OVRO, and VRO by switching the input of a single receiver between two orthogonally polarized feed outputs. At NRAO, orthogonal linear polarized feed outputs were amplified using two receivers, and the two circularly polarized signals were generated using an IF polarimeter. At the other stations, standard circular polarizers with quarter-wave plates were used. In addition, the stations at NRAO and GRAS reversed the phase of their switching cycle every 15 minutes, allowing us to measure both the visibility in like-handed polarizations (RCP × RCP denoted RR and LCP × LCP denoted LL), and also the visibility in the cross-handed polarizations (RCP × LCP denoted RL and the LCP × RCP denoted LR) for baselines that included one of these two stations.

We processed data on nine baselines, for which the (u, v) coverage for the RR and LL correlations is shown in Figure 1*a*. The response of a point source (dirty beam) to this (u, v) coverage is shown in Figure 2*a*. The central lobe is well defined with full widths at half-maximum of 0″.008 and 0″.006 and a position angle of about 145° (E of N). The largest sidelobe is about 30% of the peak of the central lobe, and the typical sidelobes are 10% of the peak across the 2″ field. For the cross-polarized measurements, RL and LR, however, we had only five baselines, for which the (u, v) coverage is shown in Figure 1*b*. The response of a point source (dirty beam) to this (u, v) coverage is shown in Figure 2*b*. The full width at half-maximum of the central lobe is 0″.010 by 0″.009 with a position angle of 145° (E of N). The largest sidelobe is also about 30% of the peak of the central lobe, and typical sidelobe levels are again 10% across the 2″ field.

b) Calibration

First, we calibrated the instrumental effects introduced by each radio telescope when measuring a particular polarization with a given feed. We then calibrated our raw data for all other instrumental effects, including antenna gain, system temperature, clock error, instrumental phase shift, differential phase shift across the receiving band, atmosphere time delay, etc. These procedures are described in Reid *et al.* (1980). We also calibrated the data to correct for instrumental phase differences between the right and left circularly polarized receiving systems.

Following the analysis of Hjellming (1978), we let the output voltage of a receiver system be expressed as

$$R_k = [G_{R_k} E_{R_k} e^{-j\theta_k} + D_{R_k} E_{L_k} e^{j\theta_k}] e^{j\omega t} \qquad (1a)$$

$$L_k = [G_{L_k} E_{L_k} e^{j\theta_k} + D_{L_k} E_{R_k} e^{-j\theta_k}] e^{j\omega t} , \qquad (1b)$$

where $G_{R_k} = A_{R_k} e^{-j\alpha_k}$, $G_{L_k} = A_{L_k} e^{j\alpha_k}$ are the antenna receiver system gains at station k when observing right and left circularly polarized radiation; D_{R_k} and D_{L_k} are the antenna receiver gains for the unwanted left and right circularly polarized radiation when observing right and left circularly polarized incoming radiation, respectively; E_R and E_L are the electric field amplitudes for the components of right and left circularly polarized incident wave at angular frequency ω; θ_k is the parallactic angle of antenna k; A_{R_k} and A_{L_k} are the antenna receiver system amplitude responses to right and left circular polarized

---

[1] The National Radio Astronomy Observatory is operated by Associated Universities Inc., under contract with the National Science Foundation.

TABLE 1

Parameters of Antennas Used in VLBI Experiment

Station	Frequency Standard	Receiver/$T_{\rm sys}$ (K)	Diameter	Mounting
Fort Davis (GRAS)	maser	paramp/110	26 m	equatorial
Green Bank (NRAO)	maser	cooled paramp/65	43 m	equatorial
Haystack (HAYS)	maser	paramp/150	37 m	alt-az
Owens Valley (OVRO)	maser	paramp/85	40 m	alt-az
Vermillion River (VRO)	rubidium	paramp/90	37 m	equatorial
Dwingeloo, Netherlands[a]	rubidium	paramp/100	25 m	alt-az

[a] Not used in polarization analysis.

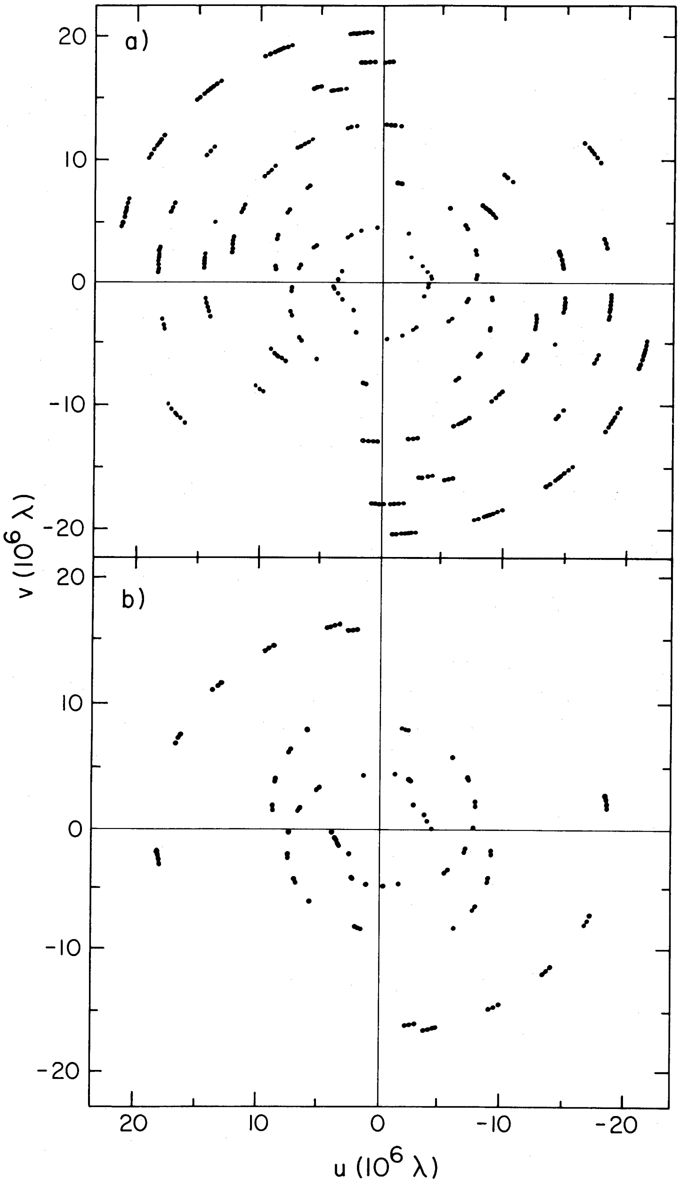

FIG. 1.—(*a*) (*u*, *v*) coverage for the RR and LL observations. (*b*) (*u*, *v*) coverage for the RL and LR observations.

incident waves; and α_k is the antenna receiver system phase response.

The fringe amplitudes and phases are derived from correlation of the form $x_i y_j^*$, where x_i and y_j are the right or left circularly polarized complex quantities of equations (1a) and (1b). Mapping of strong polarized features showed that the *D*-terms were less than 0.1 for all antennas (i.e., the power rejection was better than 20 dB), and we neglected the *D*-terms in the present analysis. With this simplification, the interferometer cross-power products are of the form:

$$x_i y_j^* = G_{x_i} G_{y_j} E_{x_i} E_{y_j} e^{\Phi_{x_i y_j}} , \qquad (2)$$

where $\Phi_{x_i y_j}$ is the phase of the cross-power function. The magnitudes of the cross-power function were calibrated by using the autocorrelation spectra from each circularly polarized receiver of each telescope. The flux density scale is based upon the auto-correlation spectra from the NRAO 43 m telescope with an assumed point-source response of 3.6 Jy K^{-1} and system temperatures measured with respect to a noise tube that was calibrated by placing known temperature absorbers in front of the feed. The right and left circularly polarized interferometer data were calibrated individually, assuming the same system temperature and aperture efficiency for both polarizations for the NRAO 43 m telescope. Observations of the unpolarized continuum source 3C 84 resulted in the same cross-correlation coefficients in right and left circular polarizations to better than 5%.

For an unpolarized point source, the phase difference of the

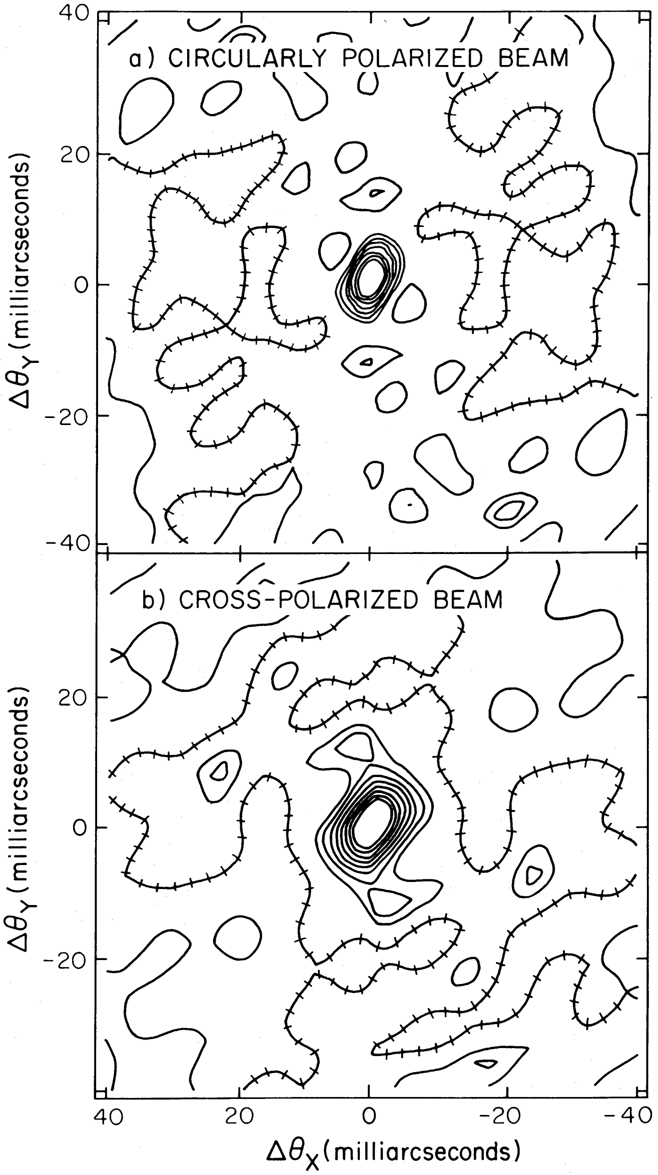

FIG. 2.—(*a*) Response to a point source (dirty beam) for the (*u*, *v*) coverage of the RR and LL observations. The major and minor axes of the dirty beam (FWHM) were 8 and 6 mas, respectively. The position angle of the major axis was 145°. The contour levels are −10, 10, 30, 40, 50, 60, 70, 80, and 90% of the peak. (*b*) Response to a point source (dirty beam) for the (*u*, *v*) coverage of the RL and LR observations. The major and minor axes of the dirty beam (FWHM) were 10 and 9 mas, respectively. The position angle of the major axis was 145°.

RR and LL correlations can be expressed as

$$(\Phi_{\mathrm{RR}} - \Phi_{\mathrm{LL}}) = -2[\theta_2(t) - \theta_1(t)] - [\alpha_2 - \alpha_1]\,, \qquad (3)$$

where Φ_{RR} and Φ_{LL} are the cross-correlation phases for the right and left circular polarization (Moran 1976). Thus, for an unpolarized point source, the peak of the correlation function for both $R_1 R_2{}^*$ and $L_1 L_2{}^*$ will have a phase difference caused by rotation of the feeds with respect to the source parallactic angles, θ_1 and θ_2 (for alt-az mounted telescopes) modified by the phases α_1, α_2, which are instrumental effects, and by propagation through the ionosphere. All data were corrected for the parallactic angle differences between telescopes, and the values of α were determined from the visibility data from 3C 84 (which we assumed to be unpolarized). We used only the visibility data from baselines involving the NRAO station (to which we arbitrarily assigned a zero phase) and derived the corresponding instrumental phase for all other stations. Since our phase reference for the maser data was a right circularly polarized feature (see below), this phase difference was removed from the LL correlation. As a check on the magnitude of the time variations of the instrumental and ionospheric phase difference, we noted that the calibrated RR* and LL* correlations for 3C 84 differed by less than $\pm 10°$ of phase over the period of the observations.

After the above corrections had been applied, the final calibration of the cross-correlation phases could proceed. An unresolved spectral feature was chosen as a phase reference. The phases of the RR* and LL* correlations were derived by referencing the phase data to the -43.78 km s^{-1} feature in the RCP spectrum. This feature was chosen as a reference because it was strong, spectrally isolated, and it appeared nearly unresolved. Phase referencing of the "cross-handed" RL* and LR* correlation utilized the -45.1 km s^{-1} feature, which exhibited strong elliptical polarization. This calibration procedure shifts the origin of the cross-polarized maps to the position of the cross-polarized reference channel and rotates the plane of polarization to that of the reference feature. The expressions for the cross-polarized interferometer phases after these adjustments become:

$$\Phi_{\mathrm{RL}_C} = \omega\,\Delta\tau_{\mathrm{off}} + 2\chi - 2\chi_{\mathrm{ref}} \qquad (4a)$$

$$\Phi_{\mathrm{LR}_C} = \omega\,\Delta\tau_{\mathrm{off}} - 2\chi + 2\chi_{\mathrm{ref}}\,, \qquad (4b)$$

where Φ_{RL_C} and Φ_{LR_C} are the calibrated phases of the cross-polarized products; $\Delta\tau_{\mathrm{off}}$ is the delay due to position offset of an individual feature; χ is the polarization position angle of the given feature; and χ_{ref} is the polarization position angle of the reference feature. The registration of the cross-polarized (Q and U) maps with respect to the circularly polarized (RR and LL) maps was accomplished by aligning the cross-polarized maps to the position of the elliptically polarized reference channel as seen in the circularly polarized maps. The polarization position angle of the cross-polarized reference channel was determined from single dish observations using the NRAO 43 m telescope to be 78° ± 2° (E of N); therefore, the values of polarization position angle given in Table 2 are those measured from the referenced maps plus 78°. This reference feature had a nearly identical position angle of 71° in 1968 (Coles, Rumsey, and Welch 1968).

c) Mapping

The calibration procedures give a complete set of correlations (RR*, LL*, RL*, and LR*) from which maps of the maser can be derived. These maps show the intensity and polarization structure as a function of sky position (x, y) relative to the reference feature. The four Stokes parameters $I(x, y)$, $Q(x, y)$, $U(x, y)$, and $V(x, y)$ can be derived from the four correlation sets by forming the following linear combinations (Morris, Radhakrishnan, and Seielstad 1964*a*, *b*; Conway and Kronberg 1969):

$$\mathrm{i}(u, v) = R_1 R_2{}^*(u, v) + L_1 L_2{}^*(u, v)\,, \qquad (5a)$$

$$\mathrm{q}(u, v) = L_1 R_2{}^*(u, v) + R_1 L_2{}^*(u, v)\,, \qquad (5b)$$

$$\mathrm{u}(u, v) = j[L_1 R_2{}^*(u, v) - R_1 L_2{}^*(u, v)]\,, \qquad (5c)$$

and

$$\mathrm{v}(u, v) = L_1 L_2{}^*(u, v) - R_1 R_2{}^*(u, v)\,. \qquad (5d)$$

The Fourier transforms of equations (5a), (5b), (5c), and (5d) yield the desired Stokes parameter maps $I(x, y)$, $Q(x, y)$, $U(x, y)$, and $V(x, y)$.

All maps were made by a two-dimensional Fast Fourier transformation of the (u, v) data and "cleaned" using the Caltech package described by Readhead and Wilkinson (1978). When cleaning maps of RCP, LCP, or Stokes parameter I, we used the standard program CLEAN, whereas when cleaning Q, U, or V maps we used a modified program that contained no restriction as to the magnitude of negative values to be subtracted. The maps were then restored using a two-dimensional Gaussian beam having a full width at half-maximum of 0".008, except for regions 4 and 5, where we used a 0".004 beam size. The cell size used was 0".002. An example of synthesized images in region 4 are shown in Figure 3.

III. RESULTS

All OH emission is seen projected onto the western half of the H II region and coinciding with the thermal NH_3 absorption (Reid, Myers, and Bieging 1987). Note that some of the maser spots lie outside the 10% intensity level of the continuum emission at 23 GHz (e.g., Fig. 7 and Dreher and Welch 1981). The overall size of the OH maser complex is about 1" × 2", elongated in the north–south direction. The individual maser spots are of the order of 5 mas in size and are frequently grouped in clumps about 30 mas across. The observed spectra in RCP and LCP polarizations obtained from the VLBI data recorded at the NRAO 140 foot (43 m) telescope are given in Figure 4. The single-dish spectra for individual Stokes parameters measured in 1980 at the NRAO 43 m telescope are shown in Figure 5. We detected maser emission from 81 different spectral features in 16 subregions (see Fig. 6). Most of these subregions are the same as those mapped by Reid *et al.* (1980). Thirty-nine features were in the northern part, 12 were at intermediate declinations, and 30 at southern declinations. The derived parameters of these features are listed in Table 2. The positions agree well with those of Reid *et al.* (1980) measured from data acquired 2.5 yr earlier. Norris and Booth (1981) suggested that the -43.78 km s^{-1} feature is moving in declination with respect to the -45.11 km s^{-1} feature at a rate of 2.1 mas yr^{-1}, which corresponds to 25 km s^{-1} at a distance of 2.5 kpc. A comparison among the data of Harvey *et al.* (1974) from 1970, Reid *et al.* (1980) from 1976, and our data from 1978 suggests that the relative motion of these two features is less than 10 km s^{-1}, which is reasonable since the spread in radial velocities is only 10 km s^{-1}.

Our map of the maser emission along with polarization

TABLE 2

1665 MHz MASERS IN W3(OH)

Velocity[a] (km s^{-1})	$\Delta\theta_x$[b]	$\Delta\theta_y$[b]	Δv[c] (km s^{-1})	$\theta_{\rm app}$[d] (mas)	PA[e]	S_ν[f] (Jy)	I[g]	Q[g]	U[g]	V[g]	χ_E[h]	m_L[i]	m_C[j]	m_T[k]
								(10^{11} K)						
Map Subregion 1[l]														
−44.18	−0″.420	−1″.820	0.40	3	...	2	1.0	...	...	1.0	...	0%	100%	100%
−44.19	−0.472	−1.805	0.21	4	...	7.1	2.0	0.1	−0.3	1.8	120°	17	90	93
−44.51	−0.405	−1.830	0.22	4	...	6	1.7	...	...	1.7	...	0	100	100
−45.33	−0.456	−1.793	0.35	6	...	9	1.1	...	...	1.1	...	0	100	100
−45.88	−0.474	−1.782	0.40	7 × 4	150°	9	1.4	...	...	1.4	...	0	100	100
−45.99	−0.476	−1.780	0.36	7 × 4	160	11	1.7	...	...	1.7	...	0	100	100
−46.16	−0.502	−1.794	0.15	4	...	5	1.4	...	...	1.4	...	0	100	100
−46.28	−0.442	−1.796	0.18	4	...	3	0.7	...	...	0.7	...	0	100	100
−46.31	−0.435	−1.803	0.27	4	...	2	0.6	...	...	0.6	...	0	100	100
Map Subregion 2														
−41.54	−0.005	−0.026	0.18	3	...	6	0.7	...	...	−0.7	...	0	−100	100
−43.78[m]	0.0	0.0	0.28	4	...	42	11.4	0.7	0.1	−10.1	76	6	−88	88
−45.18	0.029	−0.001	0.24	3	...	4	1.8	...	...	1.8	...	0	100	100
−45.25	−0.020	−0.021	0.29	4 × 3	40	2	0.9	...	...	0.9	...	0	100	100
−45.32	0.024	−0.008	0.25	3	...	3	1.4	...	...	1.4	...	0	100	100
−45.32	−0.043	0.032	0.25	3	...	3	1.7	...	...	1.7	...	0	100	100
−45.39	−0.022	0.029	0.35	3	...	2	0.9	...	...	0.9	...	0	100	100
−45.49	0.052	−0.009	0.17	3	...	3	1.5	...	...	1.5	...	0	100	100
−45.50	−0.011	0.014	0.15	3	...	3	1.5	...	...	1.5	...	0	100	100
−45.85	0.050	−0.040	0.25	6 × 3	42	2	0.5	...	...	0.5	...	0	100	100
−45.87	0.030	−0.049	0.25	9 × 3	75	4	0.6	...	...	0.6	...	0	100	100
−47.32[m]	−0.002	−0.010	0.21	6 × 3	26	5	1.2	0.4	−0.2	0.2	88	36	16	41
−48.96	0.004	0.015	0.17	9 × 3	90	3	0.4	...	...	0.4	...	0	100	100
Map Subregion 3														
−41.78	0.054	−1.746	0.29	3	...	2	0.9	...	...	−0.9	...	0	−100	100
−42.18[m]	0.037	−1.739	0.31	3	...	2	0.9	...	...	−0.9	...	0	−100	100
−42.29	0.037	−1.740	0.35	3	...	2	0.9	...	...	−0.9	...	0	−100	100
−44.02	−0.021	−1.764	0.35	3	...	7	3.3	...	...	3.3	...	0	100	100
−44.16	−0.019	−1.763	0.55	5 × 3	65	6	1.9	...	...	1.9	...	0	100	100
−44.16	−0.011	−1.758	0.55	5 × 3	50	6	1.9	...	...	1.9	...	0	100	100
−45.44[m]	0.036	−1.739	0.26	6 × 3	120	4	1.1	...	...	1.1	...	0	100	100
Map Subregion 4														
−44.64	−0.891	0.079	0.15	3	...	4	2.0	0.07	0.5	−1.8	37	25	−90	93
−44.77	−0.897	0.079	0.27	4 × 3	62	12.7	4.1	0.05	0.6	−3.3	36	14	−80	82
−44.89	−0.901	0.067	0.23	3	...	67.8	33.2	6.3	4.0	−25.1	62	23	−76	79
−44.96	−0.899	0.076	0.37	3	...	29.4	14.4	4.1	2.7	−13.2	61	34	−92	98
−44.99	−0.896	0.074	0.30	3	...	19.6	9.6	2.8	1.1	−8.7	67	31	−91	96
−45.04	−0.896	0.084	0.28	3	...	13.4	6.6	1.5	0.6	−1.0	67	43	−17	51
−45.11	−0.901	0.066	0.15	3	52	6.5	3.2	1.4	−0.3	−1.1	85	44	−34	56
−45.13	−0.898	0.089	0.20	4 × 3	40	39.9	13.0	4.0	0.2	−8.1	76	31	−62	70
−45.17	−0.896	0.092	0.22	3	34	28.4	13.9	2.7	0.0	−13.5	78	20	−97	99
−45.20	−0.904	0.093	0.20	3	...	10.3	5.0	1.0	−0.6	−2.8	94	24	−56	60
Map Subregion 5														
−42.89	−0.717	−1.703	0.24	(5)	...	8	0.4	...	...	−0.4	...	0	−100	100
−42.93	−0.716	−1.696	0.15	(5)	...	5	0.9	...	...	−0.9	...	0	−100	100
−44.23	−0.682	−1.718	0.20	12 × 3	60	2	0.2	...	...	0.2	...	0	100	100
−44.29	−0.684	−1.713	0.20	10 × 3	55	3	0.4	...	...	0.4	...	0	100	100
−44.47	−0.713	−1.688	0.19	4 × 3	40	11	4.2	−0.2	1.3	1.9	30	31	45	55
−44.89	−0.704	−1.753	0.26	9 × 4	80	4	1.1	...	...	−1.1	...	0	−100	100
−45.21	−0.718	−1.687	0.27	7	...	4	0.4	...	...	0.4	...	0	100	100
−45.22	−0.737	−1.722	0.18	7 × 3	60	10	2.1	...	...	2.1	...	0	100	100
Map Subregion 6														
−41.15	−0.674	−1.887	0.34	6	...	6	0.7	...	...	−0.7	...	0	−100	100
−41.52[m]	−0.577	−1.931	0.24	7 × 4	89	8	1.2	...	...	−1.2	...	0	−100	100
−45.50[m]	−0.577	−1.932	0.21	7 × 4	88	8.3	1.3	...	...	1.3	...	0	100	100
Map Subregion 7														
−43.39[m]	−0.949	−0.133	0.21	6 × 4	40	2	0.3	...	...	−0.3	...	0	−100	100
−45.89	−0.961	−0.156	0.17	6 × 4	50	2	0.3	...	...	0.3	...	0	100	100
−45.91	−0.964	−0.166	0.15	6 × 4	65	2	0.4	...	...	0.4	...	0	100	100
−46.00	−0.980	−0.165	0.15	4	...	2	0.6	...	...	0.6	...	0	100	100
−46.01	−0.982	−0.117	0.15	6 × 3	75	2	0.5	...	...	0.5	...	0	100	100
−46.24	−0.990	−0.162	0.37	9 × 3	35	3	0.5	...	...	0.5	...	0	100	100

TABLE 2—*Continued*

Velocity[a]	$\Delta\theta_x$[b]	$\Delta\theta_y$[b]	Δv[c]	$\theta_{\rm app}$[d]	PA[e]	S_v[f]	I[g]	Q[g]	U[g]	V[g]	χ_E[h]	m_L[i]	m_C[j]	m_T[k]
(km s^{-1})			(km s^{-1})	(mas)		(Jy)		(10^{11} K)						
Map Subregion 7														
−46.26	−1.010	−0.160	0.24	7 × 3	30	10	2.1	...	...	2.1	...	0	100	100
−46.32	−1.002	−0.164	0.28	7 × 3	30	3	0.7	...	...	0.7	...	0	100	100
−46.44[m]	−0.950	−0.135	0.35	6 × 4	46	65	11.9	...	...	11.9	...	0	100	100
Map Subregion 8														
−48.52	0.043	0.351	0.32	10 × 3	75	1.7	0.3	...	...	0.3	...	0	100	100
−48.92	0.023	0.373	0.19	5 × 3	90	8	2.3	−0.1	0.1	0.5	7	6	22	23
−48.95	0.030	0.371	0.21	5 × 3	125	13	3.7	−0.0	0.7	2.5	33	18	67	70
Map Subregion 9														
−41.26[m]	−0.126	−1.210	0.30	3	...	8	3.8	...	...	−3.8	...	0	−100	100
−42.89	−0.148	−1.134	0.24	10 × 3	195	3	0.5	...	...	−0.5	...	0	−100	100
−44.77[m]	−0.126	−1.210	0.27	4 × 3	180	22	8.0	...	...	8.0	...	0	100	100
Map Subregion 10														
−45.17	−0.087	−1.400	0.21	3	...	10	4.8	...	...	4.8	...	0	100	100
−45.29	−0.092	−1.366	0.26	3	...	2	1.2	...	...	1.2	...	0	100	100
−45.29	−0.085	−1.409	0.31	10 × 3	170	2	0.4	...	...	0.4	...	0	100	100
Map Subregion 11														
−44.29	−0.818	−0.688	0.26	5 × 4	90	2.5	0.5	...	...	0.5	...	0	100	100
−44.59	−0.829	−0.698	0.15	4 × 3	50	3	1.1	...	...	1.1	...	0	100	100
−44.80	−0.852	−0.679	0.22	8	...	4	0.3	...	...	0.3	...	0	100	100
Map Subregion 12														
−42.12	−0.233	−0.722	0.16	4	...	2.1	0.6	...	...	−0.6	...	0	−100	100
−45.98	−0.212	−0.567	0.33	6 × 4	140	4	0.7	...	...	0.7	...	0	100	100
Map Subregion 13														
−41.19	−0.005	−0.120	0.21	(5)	...	10	1.7	...	...	−1.7	...	0	−100	100
−41.53	−0.045	−0.118	0.25	5 × 4	105	3	0.7	...	...	−0.7	...	0	−100	100
−46.25	−0.165	−0.074	0.27	5 × 4	35	13	2.8	...	...	2.8	...	0	100	100
Map Subregion 14														
−42.61	−0.293	−1.095	0.31	8 × 4	170	4.3	0.6	...	...	−0.6	...	0	−100	100
Map Subregion 15														
−39.28	0.016	−0.109	0.30	3	...	2	0.9	...	...	−0.9	...	0	100	100
Map Subregion 16														
−41.12	−0.184	−1.675	0.23	9 × 3	225	3	0.5	...	...	−0.5	...	0	−100	100
−41.22	−0.160	−1.823	0.15	10 × 3	70	2	0.2	...	...	−0.2	...	0	−100	100
−41.23	−0.174	−1.828	0.22	9 × 3	55	1.5	0.2	...	...	−0.2	...	0	−100	100

[a] Velocity with respect to the local standard of rest (LSR), assuming a rest frequency of 1665.4018 MHz.

[b] Angular offsets on the sky of the maser from the reference feature (−43.78 km s^{-1} in subregion 2) toward the east (θ_x) and north (θ_y). Typical uncertainties (1 σ) for the angular offsets are ±0".002.

[c] Linewidth, full width at half-maximum (FWHM) of the feature, assuming a Gaussian line profile.

[d] The apparent angular size (FWHM) given by $(\theta_m^2 - \theta_b^2)^{1/2}$, where θ_m is the measured size and θ_b is the size of the restoring beam, θ_b = 0".008 for all map regions except subregions 4 and 5, where θ_b = 0".004 was used. For noncircular brightness distributions, apparent angular sizes are given along the major and minor axes. Where no accurate size could be measured, 0".005 was assumed and given in parentheses; sizes of 0".003 are upper limits.

[e] The apparent position angle of the maser feature measured east of north.

[f] S_v, total flux density in janskys.

[g] Peak brightness temperature calculated from I and typical error in brightness temperature is about 30% of value given; for features where $\theta_{\rm app}$ = 0".003, the brightness temperature is a lower limit. The values of Q and U have not been modified to account for the position angle of the reference feature.

[h] χ_E is the polarization position angle of the plane of vibration of the electric field measured east of north. The position angles were calibrated with respect to the angle of the feature at −45.17 km s^{-1} in subregion 4 which was determined from single-dish observations.

[i] The percent of linear polarization of the maser line. m_L is defined as $m_L = 100 \times (Q^2 + U^2)^{1/2}/I$.

[j] The percent of circular polarization. $m_C = 100 \times (V/I)$.

[k] The percent of total polarization of the maser line. m_T is defined as $m_T = 100 \times (Q^2 + U^2 + V^2)^{1/2}/I$.

[l] Map subregion numbers refer to the field used in high-resolution maps.

[m] Members of a Zeeman pair.

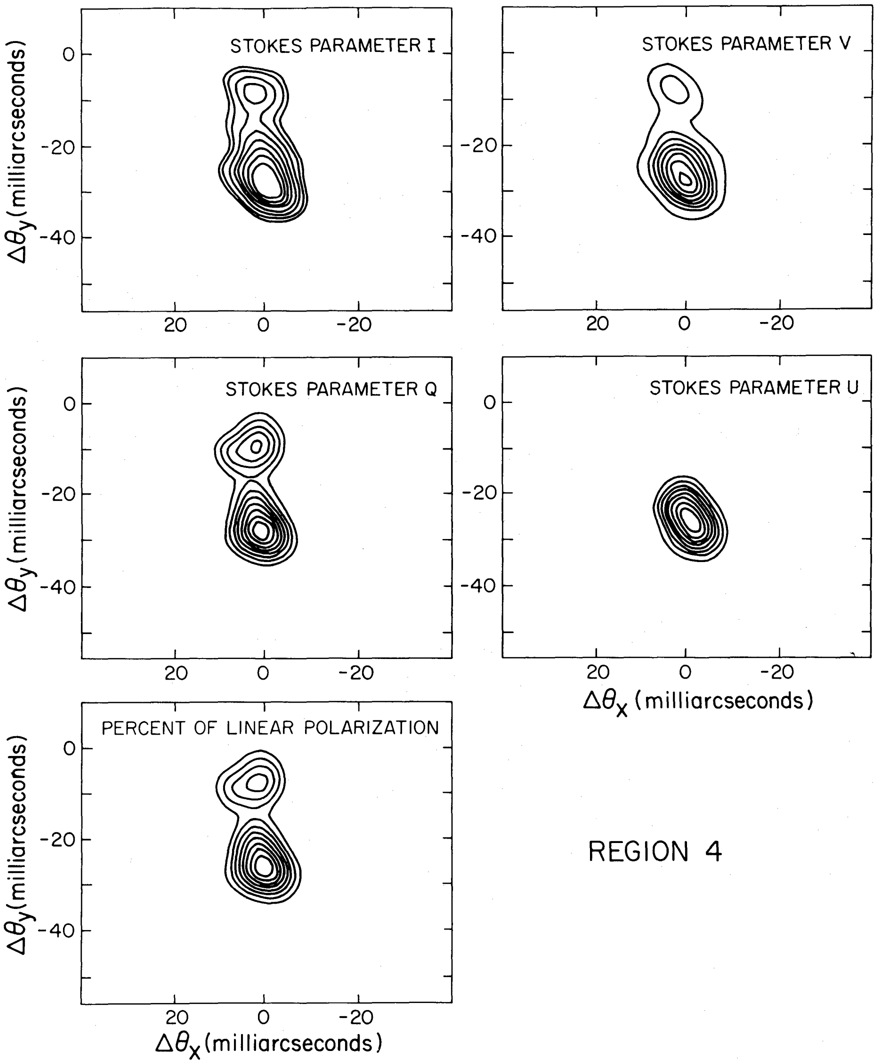

FIG. 3.—Maps of the Stokes parameters of the integrated velocity emission from subregion 4. The restoring beam had a width (FWHM) of 8 mas.

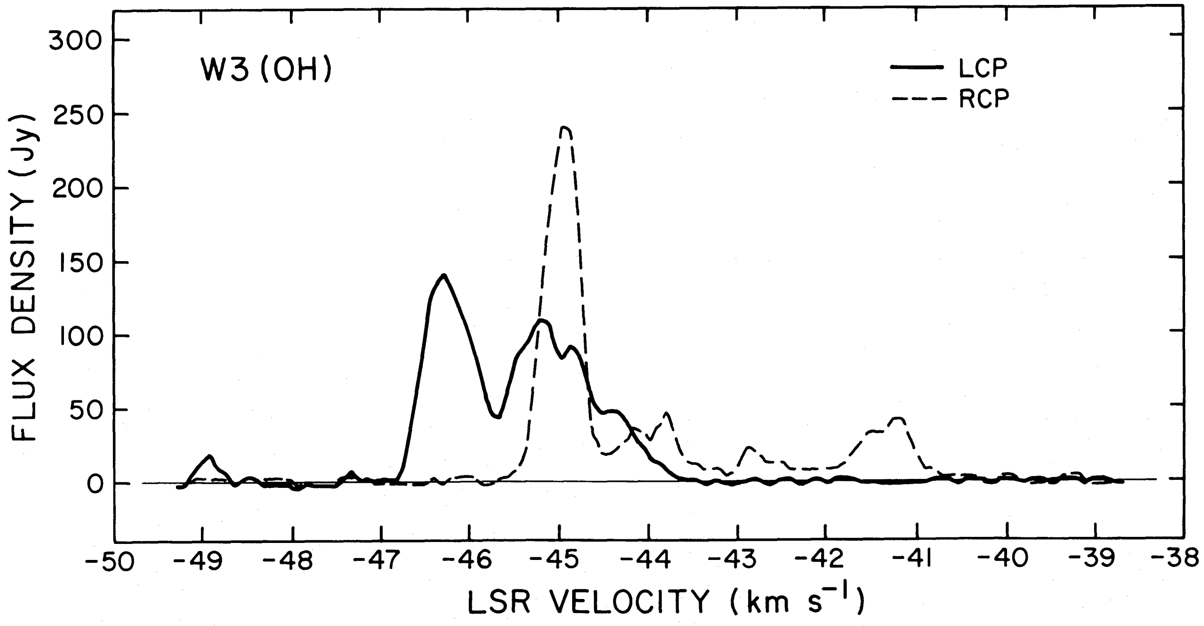

FIG. 4.—Single-antenna spectra of the right and left circular polarization of the maser emission at 1665 MHz ($^2\Pi_{3/2}$, $J = 3/2$, $F = 1$–1 transition) from W3(OH)

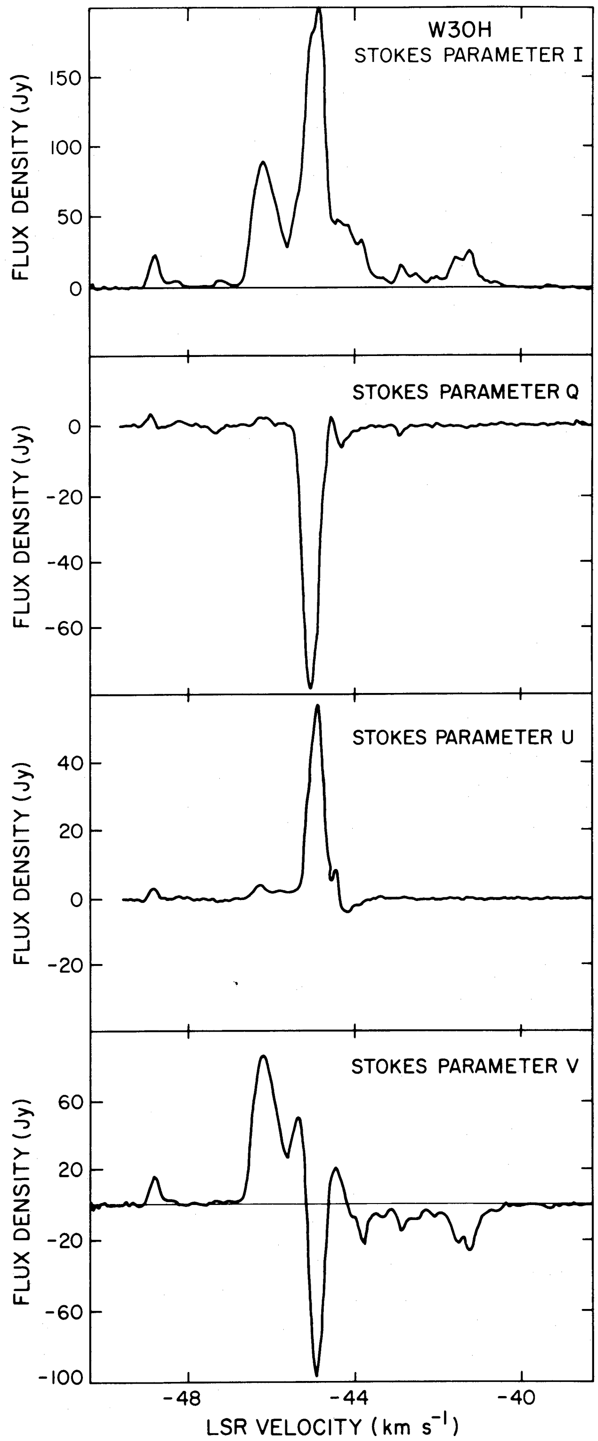

FIG. 5.—Single-antenna spectra of the Stokes parameters *I*, *Q*, *U*, and *V* of the OH maser emission from W3(OH), as observed at NRAO in 1980.

information is shown in Figure 7. The degree of polarization, defined as $m_C = V/I$ (circular) and as $m_L = (Q^2 + U^2)^{1/2}/I$ (linear) is displayed in Figure 8*a*. Were all features completely polarized, they would lie along the locus $(m_C{}^2 + m_L{}^2)^{1/2} = 1$, indicated by the dashed line. Although a large number (80%) of the features exhibit complete circular polarization, it is clear that 11 of the 16 elliptically polarized features are not completely polarized. Figure 8*b* exhibits the north–south distribution of features according to the degree of linear polarization. It can be seen that features with measurable linear polarization (i.e., elliptically polarized components) appear only in the northern or southern part of the OH emission region, while features with no linear polarization ("pure" circularly polarized components) appear at all declinations. The polarization position angles of the electric field of the elliptically polarized features varied from 7° to 120° (E of N) depending on the particular feature.

Sixty-five features showed "pure" circular polarization. From these, 46 were left circularly polarized, and 19 were right circularly polarized.The velocity full width at half-maximum was found to be in the range from 0.15 km s^{-1} to 0.55 km s^{-1}, but there is no clear correlation with circular or elliptical polarization or with strength. We were able to detect five different Zeeman pairs that appeared in subregions 2, 3, 6, 7, and 9. The parameters of the features that formed the Zeeman pairs are given in Table 3. The magnitude of the magnetic field, calculated from the velocity separation of the features, ranges from 5 to 6.5 mG with the field always pointing away from Earth. The field is somewhat more homogeneous than that deduced by Moran *et al.* (1978).

IV. DISCUSSION

The data presented in § III, as summarized in Tables 2 and 3, demonstrate an ordering of the magnetic field and provide information on the kinematics of the complex. The magnitudes of the inferred magnetic fields are surprisingly uniform. The

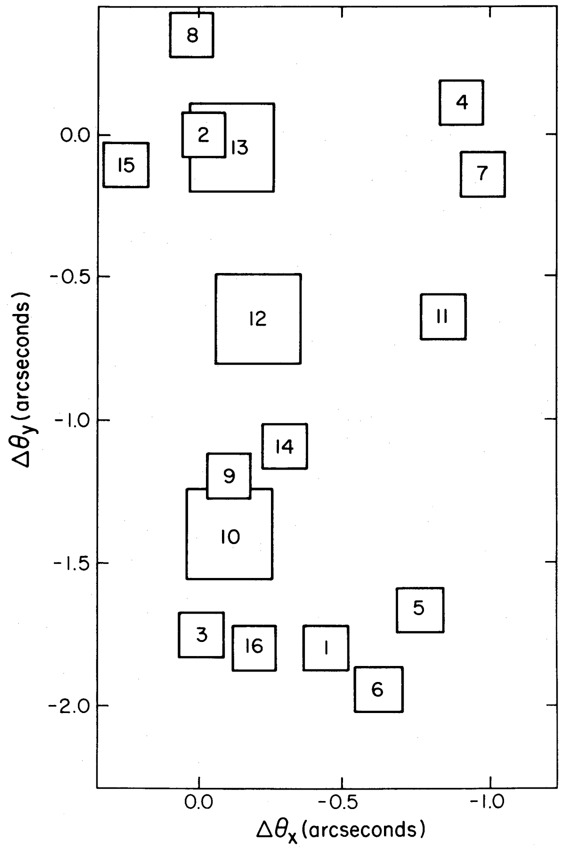

FIG. 6.—Spatial distribution of the subregions of W3(OH) at 1665 MHz in which OH maser emission was detected.

1988ApJ...326..954G

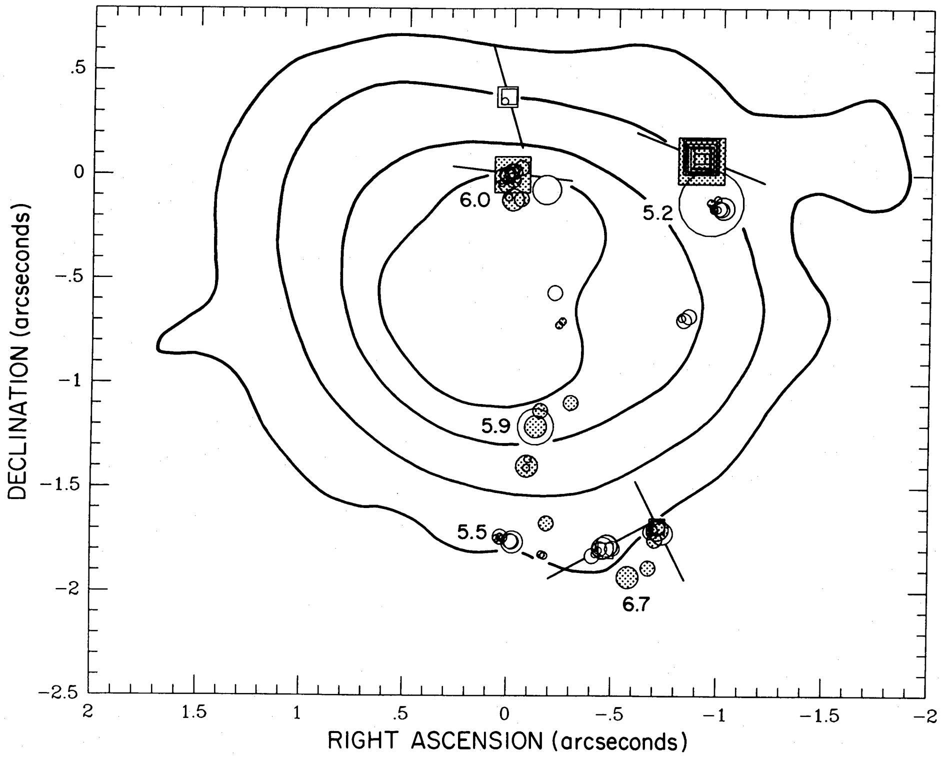

FIG. 7.—A map of the distribution of OH maser features superposed on the 23 GHz continuum emission map of Reid, Myers, and Bieging (1987). The absolute alignment between masers and continuum is taken from Reid *et al.* (1980). The solid lines are the 1, 10, 40 and 70% contours of the continuum emission. Circles show circularly polarized features (*open* are LCP; *stippled* are RCP). Squares show elliptically polarized features (*open* are LEP; *stippled* REP). The numbers on the figure are the magnetic field strength in milligauss deduced from identified Zeeman pairs (see Table 3).

observation of purely circularly and elliptically polarized components give, in principle, the possibility of tracing the three-dimensional orientation of the field in particular cases, and the data are sufficiently complete to describe the line-of-sight velocity field traced by the masing regions.

a) Strength of the Magnetic Field

The observed magnetic field strength, derived from the frequency splitting of the five detected Zeeman pairs, ranged from 5 to 6.5 mG, always pointing away from the observer. These values are consistent with previous observations (Moran *et al.* 1978; Reid *et al.* 1980) and are close to what we might expect from a microgauss interstellar magnetic field whose flux was mostly conserved in the process of contraction. If n_e scales as B^2 (e.g., Mouschovias 1976), a magnetic field enhancement of $\sim 10^4$ would yield a density enhancement of 10^8.

Two of the Zeeman pairs were detected in the north, one near the middle, and two others in the south of W3(OH). These observations suggest that the whole OH maser emission region is permeated by a magnetic field of relatively uniform strength.

b) The Elliptically Polarized Features

We next consider the evidence bearing on the vector orientation of the magnetic field. The projection of the magnetic field on the plane of the sky can be determined from the polarization position angle of the elliptically polarized features. For a π component, the projected angle of the magnetic field on the plane of the sky is parallel to its polarization angle. However, for a σ component (that exhibits elliptical polarization), the projected angle that the magnetic field makes on the plane of the sky will be perpendicular to its polarization position angle (see Fig. 9). Table 2 lists the properties of features that showed elliptical polarization.

Two interesting aspects of our data are shown in Figures 8*a* and 8*b*. First, none of these features is 100% polarized. As noted in § III, any features with 100% polarization would trace a circle in a plot of m_C versus m_L (see Fig. 8*a*). There are several possible explanations: (1) circular polarization was inhibited (they should have higher percentage of circular polarization); (2) linear polarization was inhibited (they should have higher percent of linear polarization), (3) each feature observed is composed of two features blended in velocity, one with "pure" circular and one with "pure" linear polarization; and (4) each feature observed is composed of three features blended in velocity, one with "pure" circular, one with "pure" linear polarization, and one unpolarized. For the last two possibilities, one would expect to observe larger linewidths and sizes for features exhibiting elliptical polarization than for features with only "pure" circular polarization. This is not observed; linewidths and sizes of the elliptically and circularly polarized features are comparable.

The observations suggest that features with elliptical polarization are "single" spectral lines and that they are σ components. Only in highly unlikely cases of velocity gradients and magnetic field strength could one expect to see a circularly polarized π component (caused by line overlap of σ and π components, which are amplified in different portions of the maser). Generally, π components can be either linearly polarized or unpolarized. No such components are observed. If this conclusion is correct, one needs to explain why the σ components are partially polarized and no π components are detected. The theory of Goldreich, Keeley, and Kwan (1973*a*,

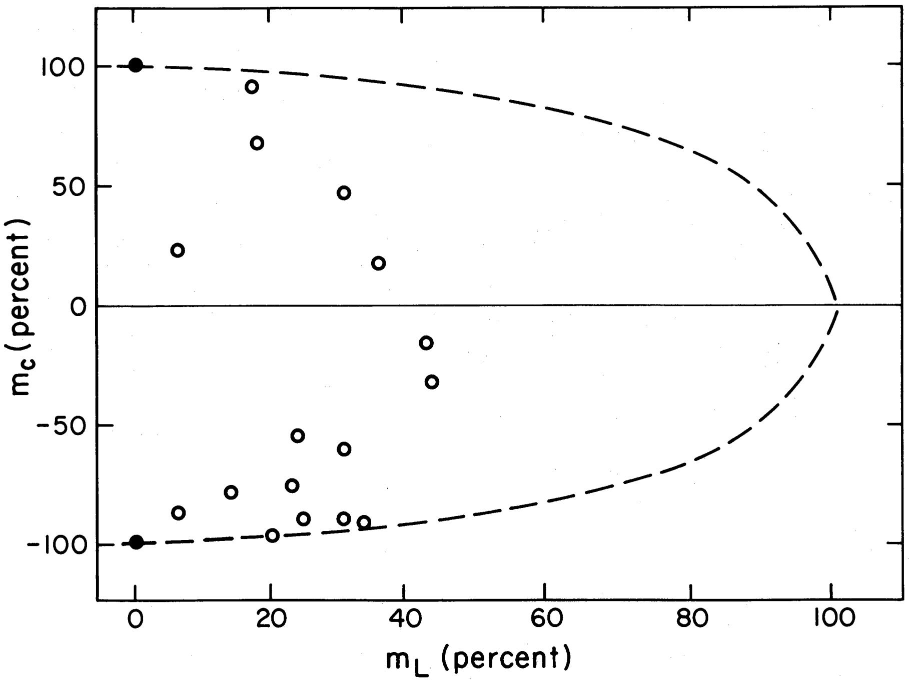

FIG. 8*a*

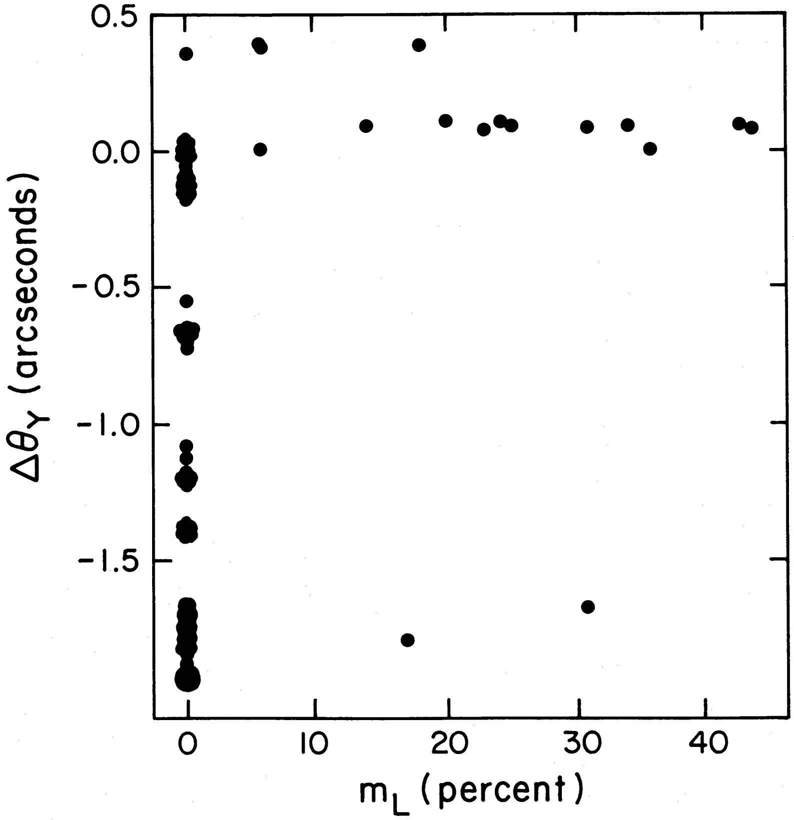

FIG. 8*b*

FIG. 8.—(*a*) Percentage of linear vs. circular polarization of each feature. Filled dots at $m_C = 100$ and $m_C = -100$ represent features with "pure" left and right circular polarization, respectively. There were 46 features with "pure" left circular polarization and 19 features with "pure" right circular polarization. For a completely polarized feature $m_T = [m_C^2 + m_L^2]^{1/2} = 100$. This condition is indicated by the dashed line. The horizontal scale is approximately twice the vertical scale to emphasize the distribution observed. (*b*) The declination vs. percentage of linear polarization for maser features. All features with $m_L = 0$ represent the circularly polarized components. Notice that the features with nonzero percentage of linear polarization lie either at the northern or southern part of the OH emission region but not at intermediate declinations.

TABLE 3

1665 MHz ZEEMAN PAIR MASERS IN W3(OH)

Velocity[a] (km s^{-1})	$\Delta\theta_x$[b]	$\Delta\theta_y$[b]	Δv[c] (km s^{-1})	θ_{app}[d] (mas)	PA[e]	S_ν[f] (Jy)	T_B[g] (10^{11} K)	Polarization[h]	Velocity[i] (km s^{-1})	B[j] (mG)
				Map Subregion 2[k]						
−43.78........	0″.0	0″.0	0.28	4	...	42	11.4	RCP	3.54	6.0
−47.32.........	−0.002	−0.010	0.21	6 × 3	26°	5	1.2	LCP		
				Map Subregion 3						
−42.18.........	0.037	−1.739	0.31	3	...	2	0.9	RCP	3.26	5.5
−45.44.........	0.036	−1.739	0.26	6 × 3	120	4	1.1	LCP		
				Map Subregion 6						
−41.52.........	−0.577	−1.931	0.24	7 × 4	89	8	1.2	RCP	3.98	6.7
−45.50.........	−0.577	−1.932	0.21	7 × 4	88	8.3	1.3	LCP		
				Map Subregion 7						
−43.39.........	−0.949	−0.133	0.21	6 × 4	40	2	0.3	RCP	3.05	5.2
−46.44.........	−0.950	−0.135	0.35	6 × 4	46	65	11.9	LCP		
				Map Subregion 9						
−41.26.........	−0.126	−1.210	0.30	3	...	8	3.8	RCP	3.51	5.9
−44.77.........	−0.126	−1.210	0.27	4 × 3	180	22	8.0	LCP		

[a] Velocity with respect to the local standard of rest (LSR), assuming a rest frequency of 1665.4018 MHz.

[b] Angular offsets on the sky of the maser from the reference feature (−43.78 km s^{-1} in subregion 2) toward the east (θ_x) and north (θ_y). Typical uncertainties (1 σ) for the angular offsets are ±0″.002.

[c] Linewidth, full width at half-maximum (FWHM) of the feature, assuming a Gaussian line profile.

[d] The apparent angular size (FWHM) given by $(\theta_m^2 - \theta_b^2)^{1/2}$, where θ_m is the measured size and θ_b is the size of the restoring beam, θ_b = 0″.008 for all map regions except subregions 4 and 5, where θ_b = 0″.004 was used. For noncircular brightness distributions, apparent angular sizes are given along the major and minor axes. Where no accurate size could be measured, 0″.005 was assumed and given in parentheses; sizes of 0″.003 are upper limits.

[e] The apparent position angle of the maser feature measured east of north.

[f] S_ν, total flux density in janskys.

[g] Peak brightness temperature calculated from I and typical error in brightness temperature is about 30% of value given; for features where θ_{app} = 0″.003, the brightness temperature is a lower limit. The values of Q and U have not been modified to account for the position angle of the reference feature.

[h] Instrinsic polarization shown by the maser feature, IEEE convention. RCP stands for right circular polarization; LCP stands for left circular polarization.

[i] Velocity difference between the σ^+ and σ^- of the components of the Zeeman pairs. A velocity splitting of 0.59 km s^{-1} is produced by a magnetic field of strength of 1 mG (see Fig. 9).

[j] Magnetic field deduced from the velocity difference observed between the components of the Zeeman pairs. The magnetic field points away from Earth in all cases.

[k] Map subregion refers to number of the field used in high-resolution maps.

b) suggests an answer: in order for σ components to be partially polarized it is required that Faraday rotation, intrinsic to the cloud where OH emission originates, be important over the path length, together with resonant trapping of infrared radiation that allows a cross-relaxation among magnetic sublevels. The Faraday rotation across a region of length L with longitudinal magnetic field $B_\parallel$ and electron density n_e is (e.g., Thompson, Moran and Swenson 1986)

$$\psi = 0^\circ.5\left(\frac{n_e}{\mathrm{cm}^{-3}}\right)\left(\frac{B_\parallel}{\mathrm{mG}}\right)\left(\frac{L}{10^{15}\ \mathrm{cm}}\right)\left(\frac{\lambda}{18\ \mathrm{cm}}\right)^2 . \tag{6}$$

Hence, for a total amplification length of 2×10^{15} cm and longitudinal magnetic fields of 5 mG, an electron density n_e = 70 cm^{-3} is required to give 360° of rotation across the maser region. Such an electron density is reasonable if the masers exist in the C II region outside the Strömgren radius. In this region, the fractional ionization is about equal to the cosmic [C]/[H] ratio of $\sim 10^{-4}$. Hence, if the neutral density is $\sim 10^6$ cm^{-3}, the ionized density would be $\sim 10^2$ cm^{-3}, as required for depolarization. The second observational property to be explained is the lack of features with elliptical polarization at intermediate declinations. The elliptically polarized features seem to originate either from the northern or southern regions (see Fig. 8*b*). This characteristic could be explained by large differential Faraday rotation and/or magnetic field orientation at intermediate declinations. If all OH masers have the same amplification length, one would require a higher electron density at intermediate declinations to enhance Faraday effects. Conversely, if one assumes a constant electron density across the whole cloud then one requires slightly larger amplification lengths at intermediate declinations.

The total magnetic field can be readily estimated from the Zeeman splitting of the lines. However, it is much more difficult to estimate the orientation of the field. It may be possible to deduce the orientation of the field from our measurements of elliptical polarization if several assumptions are made. The elliptically polarized features are probably σ components because π components are normally linearly polarized. Only under very unusual conditions can the π components have any circular polarization. Hence, in the absence of Faraday rotation, the projected orientation of the magnetic field would be orthogonal to the plane of elliptical polarization. Internal Faraday rotation rotates the plane of polarization and reduces the degree of polarization. However, in subregion 4 there are elliptically polarized features that are more than 95% polarized. The polarization position angle in this subregion is 65° ± 30°. Note that there is a monotonic trend in position angle with frequency, which may be evidence for magnetorotation (Goldreich, Keeley, and Kwan 1973*a*). The high degree of polarization suggests that the internal Faraday rotation is small. If there is no external Faraday rotation between the maser and us, then the inferred field position angle would be 155° ± 30°.

The angle that the magnetic field makes with respect to the line of sight depends on the maser model and degree of saturation. Goldreich, Keeley, and Kwan (1973*a*, *b*) predict intensities of the Stokes parameters in terms of the angle that the magnetic field makes with the line of sight, θ. The masers are probably saturated. Their estimate of the cross-relaxation rate for the OH molecule is 0.10 s^{-1}, and the decay rate for the energy levels involved is 0.02 s^{-1}. The microwave emission rate, R, given in terms of observable quantities is (Reid and Moran 1981)

$$R = 37.7 F_e \Omega_e / \Omega_s \ \mathrm{s}^{-1} , \tag{7}$$

where F_e is the flux density of the line in janskys, Ω_e is the beam solid angle of microwave emission in steradians, and Ω_s is the apparent maser source size in square milliarcseconds. For $F_e = 30$ Jy, $\Omega_s = 9$ mas^2 and assuming $\Omega_e = 10^{-2}$ steradians, we obtain $R = 1.2$. Given that the decay rate is almost two orders of magnitude smaller than the stimulated emission rates for most of the features observed, we adopt a saturated maser model. In subregions 1, 2, and 5, we detected elliptically as well as purely circularly polarized features. In subregion 2, we detected circularly polarized components and a Zeeman pair, while in subregion 4 we only detected elliptically polarized components. Other subregions (i.e., 3, 6, 7, 9, 10, 11, 12, 13, 14, 15, and 16), exhibited nearly 100% circular polarization for nearly all maser components, and the angle of the magnetic field to the line of sight (for σ components to dominate) must be less than 72°. If the maser model is correct, this is the first derivation of a three-dimensional picture of the magnetic field in a star formation region.

Four subregions deserve special attention, namely, subregions 2, 4, 5, and 8. Subregion 2 shows, among other lines, two components, previously detected by Norris and Booth (1981), coming from the same maser clump forming a Zeeman pair. These σ lines showed elliptical polarization, in contrast with other components of the other Zeeman pairs that showed "pure" circular polarization. Subregion 4 is special in the sense that we only detected elliptically polarized components and

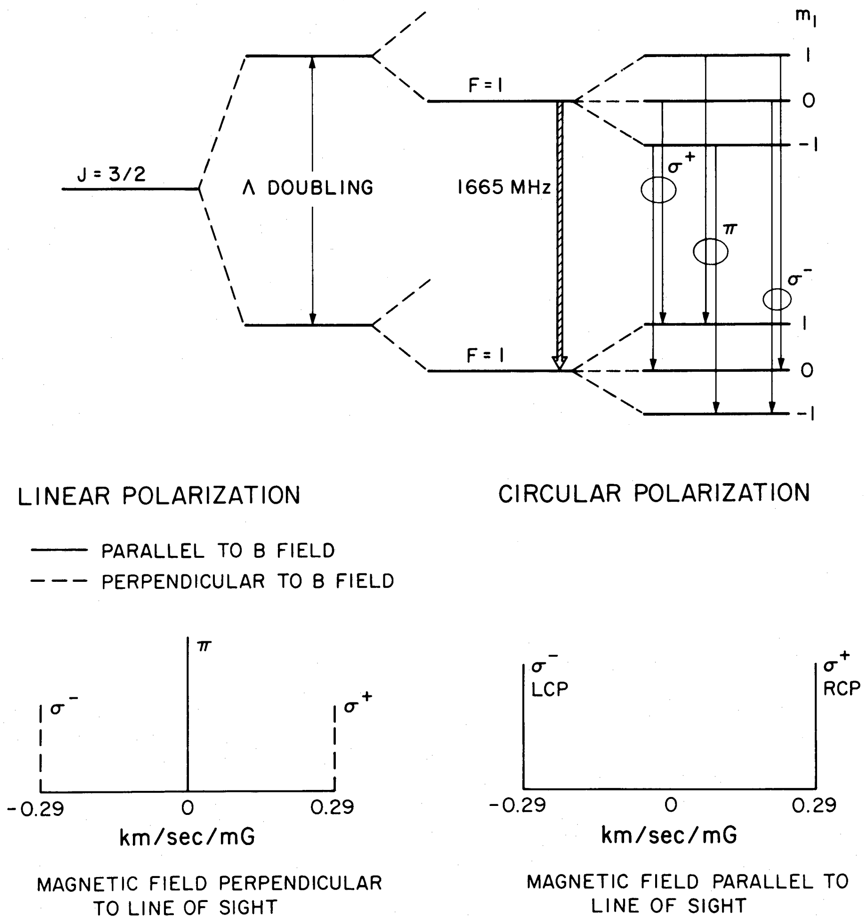

FIG. 9.—Energy levels of the OH molecule in the $^2\Pi_{3/2}$ ground state showing the levels of the 1665 MHz line with the different transitions possible (σ or π components). Also shown is the relative strength and polarization of these features with respect to the orientation of the magnetic field with the line of sight; the figure on the lower right corresponds to the case when the magnetic field points away from Earth and is parallel to the line of sight.

the polarization position angle varied with the radial velocity, and to a lesser extent, with the flux density of the feature. The stronger features showed higher percentages of total polarization than the weaker features, but both groups have a comparable linewidth. All features had higher percentage of circular than linear polarization.

Four of the five Zeeman pairs found showed different strength for one feature compared with the other. The linewidths of each feature in a Zeeman pair was, on the average, the same as for features showing pure circular or elliptical polarization. In all of these cases, the Zeeman frequency shift was larger than the linewidth of the lines.

V. SUMMARY

We have measured the four Stokes parameters of the OH maser emission from W3(OH) using the Mark II VLBI system. These observations provided us with the means of mapping the spatial distribution of the maser emission together with their polarization properties. The percentage of linear, circular and total polarization of each spectral feature was measured. A high degree of circular polarization is common, but elliptical polarization was also observed. The elliptically polarized features occur in the northern and southern regions but avoid the central part of the maser complex. Five Zeeman pairs were detected, and these show that the magnetic field is rather uniform: 5–6.5 mG, always pointing away from Earth. The linewidth found varied from 0.15 km s^{-1} to 0.55 km s^{-1}, with no clear correlation with strength, polarization, or size of the maser feature. We note the absence of "pure" linearly polarized or unpolarized features that could be identified as π components. A combined effect of Faraday rotation, resonant trapping of infrared radiation allowing cross-relaxation among magnetic sublevels, and certain magnetic field orientations to the line of sight are required to explain the low percentage of linear polarization seen in the elliptically polarized components. The projected angle of the 6 mG magnetic field on the plane of the sky, assuming that the features that have a high degree of elliptical polarization are σ components, is generally 150° (E of N).

The magnetic field strength of the order of few milligauss is approximately what one might expect from compression of the general galactic magnetic field, although the present observations can give no indication that this is indeed the case.

J. A. G.-B. acknowledges partial financial support from CONACYT (Mexico) and also from Smithsonian Astrophysical Observatory. He would also like to thank the staff at the Radio and Geoastronomy Division of the Smithsonian Astrophysical Observatory for their continuous support and hospitality during the course of this work. The authors wish to thank A. van Ardenne for his support during the observations at Dwingeloo, G. W. Swenson for support at the Vermillion River Observatory, the staff of the other network stations (OVRO, NRAO, GRAS, and Haystack) for assistance, and R. Levreault for helpful discussions.

REFERENCES

Barrett, A. H., and Rogers, A. E. E. 1966, *Nature*, **210**, 188.
Berulis, I. I., and Ershov, A. A. 1983, *Soviet Astr. Letters.*, **9**, 6.
Coles, W. A., Rumsey, V. H., and Welch, W. J. 1968, *Ap. J.* (*Letters*), **154**, L61.
Conway, R. G., and Kronberg, P. P. 1969, *M.N.R.A.S.*, **142**, 11.
Davies, R. D. 1974, in *Galactic Radio Astronomy*, ed. F. J. Kerr and S. C. Simonson (Dordrecht: Reidel), p. 275.
Dreher, J. W., and Welch, W. J. 1981, *Ap. J.*, **245**, 857.
Garay, G., Reid, M. J., and Moran, J. M. 1985, *Ap. J.*, **289**, 681.
Goldreich, P., Keeley, D. A., and Kwan, J. Y. 1973*a*, *Ap. J.*, **179**, 111.
———. 1973*b*, *Ap. J.*, **182**, 55.
Harvey, P. J., Booth, R. S., Davies, R. D., Whittet, D. C. B., and McLaughlin, W. 1974, *M.N.R.A.S.*, **169**, 545.
Hjellming, R. 1978, *An Introduction to the VLA* (Green Bank, W. Va: NRAO).
Lo, K. Y., Walker, R. C., Burke, B. F., Moran, J. M., Johnston, K. J., and Ewing, M. S. 1975, *Ap. J.*, **202**, 650.
Meeks, M. L., Ball, J. A., Carter, J. C., and Ingalls, R. P. 1968, *Science*, **153**, 978.
Moran, J. M. 1976, in *Methods of Experimental Physics*, Vol. **12C**, ed. M. L. Meeks (New York: Academic), chap. 5.5.
Moran, J. M., Burke, B. F., Barrett, A. H., Rogers, A. E. E., Ball, J. A., Carter, J. C., and Cudaback D. D. 1968, *Ap. J.* (*Letters*), **152**, L97.
Moran, J. M., Reid, M. J., Lada, C. J., Yen, J. L., Johnston, K. J., and Spencer, J. H. 1978, *Ap. J.* (*Letters*), **224**, L67.
Morris, D., Radhakrishnan, V., and Seielstad, G. A. 1964*a*, *Ap. J.*, **139**, 551.
———. 1964*b*, *Ap. J.*, **139**, 560.
Mouschovias, T. C. 1976, *Ap. J.*, **207**, 141.
Norris, R. P., and Booth, R. S. 1981, *M.N.R.A.S.*, **195**, 213.
Norris, R. P., Booth, R. S., and Diamond, P. J. 1982, *M.N.R.A.S.*, **201**, 209.
Readhead, A. C. S., and Wilkinson, P. N. 1978, *Ap. J.*, **223**, 25.
Reid, M. J., Haschick, A. D., Burke, B. F., Moran, J. M., Johnston, K. J., and Swenson, G. W., Jr. 1980, *Ap. J.*, **239**, 89.
Reid, M. J., and Moran, J. M. 1981, *Ann Rev. Astr. Ap.*, **19**, 231.
Reid, M. J., Myers, P. C., and Bieging, J. H. 1987 *Ap. J.*, **312**, 830.
Thompson, A. R., Moran, J. M., and Swenson, G. W. 1986, *Interferometry and Synthesis in Radio Astronomy* (New York: Wiley-Interscience), p. 460.
Troland, T. H., and Heiles, C. H. 1982, *Ap. J.*, **252**, 179.
Verschuur, G. L. 1974, in *Galactic and Extragalactic Radio Astronomy*, ed. G. L. Verschuur and K. I. Kellermann (Springer-Verlag), p. 179.
Welch, W. J., and Marr, J. 1987, *Ap. J.* (*Letters*), **317**, L21.

B. F. BURKE: Research Laboratory of Electronics, Massachusetts Institute of Technology, 77 Massachusetts Avenue, Cambridge, MA 02139

J. A. GARCÍA-BARRETO: Instituto de Astronomía, Universidad Nacional Autónoma de México, Apartado Postal 877, Ensenada, B. C., Mexico

A. D. HASCHICK: Haystack Observatory, Westford, MA 01886

J. M. MORAN AND M. J. REID: Harvard-Smithsonian Center for Astrophysics, 60 Garden Street, Mail Stop 42, Cambridge, MA 02138

R. T. SCHILIZZI: Netherlands Foundation for Radio Astronomy, Dwingeloo, The Netherlands